Received 19 October 2021; accepted 8 November 2021. Date of publication 12 November 2021; date of current version 24 November 2021.

Digital Object Identifier 10.1109/OJAP.2021.3127643

A Broadband High-Efficiency Dipole Array Based on Frequency Selective Surface and Integrated Feeding Structure

HONG TANG, BOWEN ZHENG, SENSONG AN, HANG LI, MOHAMMAD HAERINIA, CLAYTON FOWLER, AND HUALIANG ZHANG (Senior Member, IEEE)

Department of Electrical and Computer Engineering, University of Massachusetts Lowell, Lowell, MA 01854, USA

CORRESPONDING AUTHOR: H. ZHANG (e-mail: hualiang_zhang@uml.edu)

ABSTRACT In this paper, an ultra-wideband tightly couple antenna array based on a low-loss phase-modulated frequency selective surface and a microstrip-based feeding structure is reported. The proposed antenna array, which employs tightly coupled bow-tie elements, features a very low profile ($1.08\lambda_{high}$). Specifically, a microstrip-to-parallel strip transition serves as an impedance transformer and a wideband balun to enable the array element to be excited with a 50 Ω unbalanced feeding scheme. Additionally, one shorting sheet is employed to expand the bandwidth by shifting the common-mode to a higher frequency band. The presented design achieves a bandwidth of 13.66:1 (0.52 GHz – 7.10 GHz) with VSWR $<$ 2.49 and simulated radiation efficiency greater than 96% across the whole band. To validate the design concepts, an 8 $\times$ 8 array prototype is fabricated and characterized experimentally. The measured results match well with the numerical analysis.

INDEX TERMS Frequency selective surface (FSS), tightly coupled arrays (TCAs), ultra-wideband antenna arrays, wideband balun.

I. INTRODUCTION

RECENTLY, high-resolution radar systems and imaging systems are becoming more and more prevalent. To meet the stringent system requirements in terms of detection range, power level, and resolution, the antenna arrays in these systems must provide large operating bandwidth, high efficiency, and high gain. In the past, ultra-wideband antenna arrays such as the Vivaldi antenna array [1], [2], were involved in these systems [3] and [4]. Nevertheless, the elements of these arrays are not planar, have a relatively high profile, and require an elaborate feeding structure.

Compared with the conventional wideband antenna arrays, tightly coupled dipole arrays (TCDAs) are becoming more and more attractive because of their key features, such as low-profile and ultra-wideband properties [5]. In [6], a wideband current sheet antenna (CSA) array using tightly coupled dipoles arranged over a ground plane was developed. The transmission line model exhibited in [7] illustrates that the inductive reactance of the ground plane can be counteracted by the capacitive reactance of the dipole layer, resulting in a stable, mostly real input impedance over a wide bandwidth. In [8]–[10], the invented TCDAs (i.e., PUMA arrays) based on CSAs can achieve a bandwidth of 6:1 and eliminate the need for bulky cable organizers [11] and external baluns. However, the operating bandwidth of the array is still limited by the ground plane and the feeding structure.

To further improve the operating bandwidth of TCDAs, not only the inductive reactance but also the wave reflected by the ground and the feeding structure should be taken into consideration. To handle the reflection effects, new types of TCDAs are introduced in [12]–[14] realized with layers of lossy materials such as resistive sheets. Since the power reflected by the ground plane is absorbed by the resistive sheets, the operating bandwidth of the resulting antenna arrays will not be affected by the reflection and can be up to 21:1 (from 0.285 GHz to 5.92 GHz) with VSWR $<$ 3. Nevertheless, the radiation efficiency of the antenna arrays is reduced (down to 73%) because part of the radiated energy is dissipated by the lossy resistive sheets. Moreover, the thermal dissipation of these arrays is a key challenge, especially

when applied in high-power RF/microwave systems (e.g., high-power radar systems).

To increase the operating bandwidth and maintain high radiation efficiency, a novel TCDA with an operating bandwidth of 20.9:1 (from 91 MHz to 1901 MHz) based on the polarization converter (PC) is reported in [15]. The broadband PC designed with a bandwidth of 3.14:1 (from 700 MHz to 2000 MHz) can convert the polarization of the reflection from the ground plane, which will lead to broadband poor polarization purities. According to the simulated return loss of the PC presented in [15], the portion of the bandwidth with poor polarization purity (700 MHz to 1901 MHz) occupies around 66.4% of the whole operating bandwidth (91 MHz to 1901 MHz), which means most of the operating band will suffer from poor polarization purity. Additionally, the inherent ideas of how the bandwidth is enlarged and design concepts between the shorting circuit and the additional PC are not revealed. Furthermore, to feed this antenna element, a separate ultra-wideband balun chip (MABA-010247-2R1250) is adopted in this design to provide the array element with balanced feeding. Insertion loss, operating bandwidth, and power handling of the balun chip will limit the efficiency, scalability, and power handling properties of the antenna array.

Meanwhile, TCDAs in [8]–[10] are excited by the 50 Ω unbalanced feeding schemes, which is a significant limitation to further pushing the bandwidth. In [13], [14], and [16], a folded Marchand balun based on striplines is harnessed as a wideband feeding to excite the antenna element. Compared with microstrip transmission lines, striplines are more expensive to fabricate. Furthermore, they have sandwiched structures which makes them harder to be assembled with commercial surface mount connectors. Overall, the stripline-based feeding has better element coupling and impedance control, but the design concept is complex. The impedance and element coupling controllability of microstrip-based feeding is not as good as stripline-based feeding, but these issues can be accommodated well for TCDAs when the shorting structure is applied.

As presented in [17]–[19], several microstrip-based feeding schemes are presented. In [17], one microstrip-based tapered balun is adopted as the feeding structure without any shorting structure to shift the common-mode. Nonetheless, the profile of the tapered balun is large, which is around 1.93 λhigh. Notably, to further suppress the common-mode resonance, resistive loading is used in the antenna array, which will lead to low radiation efficiency and thermal issues. To realize a feeding with a small profile and without sacrificing the radiation efficiency, microstrip-based feedings with shorting structures are proposed in [18] and [19]. In [18], shorting pins are connected from the excited dipole arms to the ground plane of the array directly to shift the common-mode to higher frequencies and out of the desirable band. However, the operating bandwidth will be limited by the length of the shorting structure if the operating bandwidth is further improved (detailed in the next section). In [19], a microstrip-to-slotline transition is optimized to feed the array element. The short stub from the slotline acted as the shorting circuit to shift the common-mode to higher frequencies. The bandwidth is again limited by the length of the shorting stub.

To address these issues, a new TCDA composed of a low-loss, phase-modulated FSS and a wideband feeding structure based on the microstrip-to-parallel strip transition is introduced in this paper. The proposed FSS can modify the phase of the reflected signal coming from the ground plane rather than absorb the power so that the operating bandwidth can be significantly enlarged, while the radiation efficiency and the total radiated power will not be sacrificed. To reveal the intrinsic relationship between the topologies of the FSS, short-circuit, the polarization purity, and the operating bandwidth, the FSS with different design parameters is simulated, and the phase response and the magnitude response of the reflection are presented in the next section.

To increase the polarization purity, one PTFE-based ($\varepsilon_r = 2.1$, $tan\ \delta = 0.0004$) superstrate is designed and positioned on the top of the proposed radiating elements. Furthermore, a microstrip-based tapered balun known as microstrip-to-parallel strip transition is adopted and intended to be the feeding structure so that the proposed antenna array can be easily fed by 50 Ω unbalanced coaxial cables. To expand the operating bandwidth of the feeding structure and the antenna array, one shiftable shorting structure connected with the ground plane and the radiating element is utilized to shift the undesirable common-mode to higher frequencies (out of the operating frequency band). In this way, the designed antenna array can realize a bandwidth of 13.66:1 (0.52 GHz – 7.10 GHz) with VSWR < 2.49 and simulated radiation efficiency higher than 96% across the whole frequency band. To verify the performance of the proposed antenna array, an 8 × 8 antenna array prototype was fabricated, assembled, and characterized experimentally. Good agreements have been achieved between simulations and measurement results, validating the proposed design concepts.

This paper is organized as follows. Section II presents the geometries and design principles of the radiating element, FSS, feeding structure, and superstrate. Section III describes the numerical results of the infinite array. Full-wave finite array simulations and measurements of the 8 × 8 antenna array prototype are displayed in Section IV. Conclusions are drawn in Section V.

II. SCHEMATICS AND DESIGN PRINCIPLES

A. OVERVIEW OF THE PROPOSED ANTENNA ARRAY ELEMENTS

The topology of the array elements is depicted in Fig. 1. The total height of the antenna element is 45.67 mm ($1.08\lambda_{high}$), which is significantly lower than the Vivaldi antenna ($6.24\lambda_{high}$) [1]. As described above, the antenna array element is composed of four parts, which are a radiator, an FSS, a superstrate, and an integrated feeding structure. Specifically, the radiator is based on the broadband bow-tie antenna whose characteristic impedance is 150 Ω. The

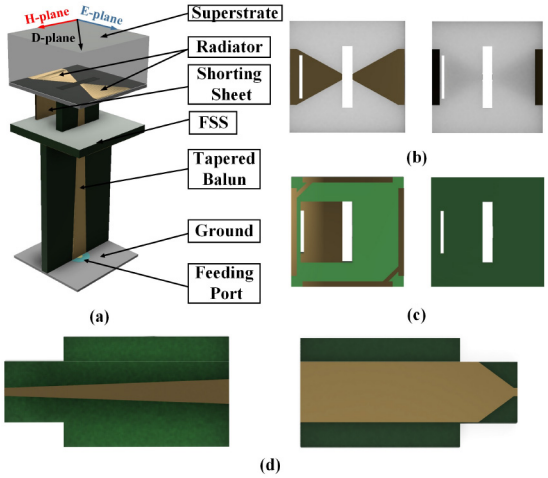

FIGURE 1. The schematics of the proposed array element. (a) Overview of the unit cell of the array element. (b) The top (left) and back (right) views of the bowtie radiator. (c) The top (right) and back (left) views of the FSS. (d) The top (left) and back (right) views of the feeding structure.

TABLE 1. Infinite array geometric parameters.

D	L	dipolegap1	dipolegap2	dipolel1
18.00 mm	36.00 mm	1.26 mm	0.13 mm	9.00 mm
dipolel2	dipolew1	feedbackl1	feedbackl2	feedbackw1
0.72 mm	0.635 mm	1.65 mm	30.00 mm	10.00 mm
feedbackw2	feedoffset	feedsubl1	feedtopl1	feedtopw1
1.35 mm	-0.653 mm	10.00 mm	36.00 mm	4.00 mm
feedtopw2	fssarmmove	d	fssl1	superthick
1.35 mm	2.50 mm	12.00 mm	14.40 mm	9.00 mm
fssw1	shortw			
0.40 mm	7.50 mm			

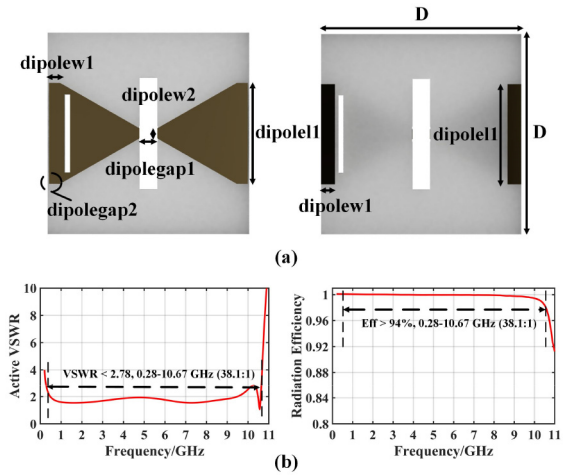

FIGURE 2. (a) The geometries of the radiator. (b) Simulation results of the radiator.

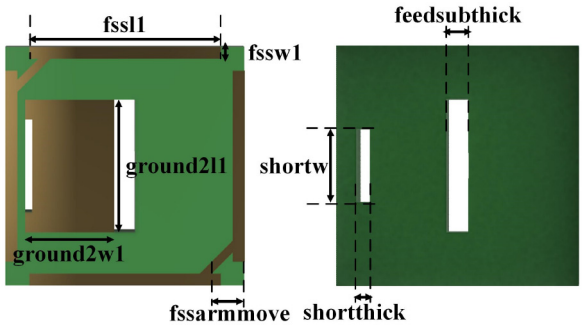

FIGURE 3. The geometries of the proposed FSS. Left: the back view of the FSS. Right: the top view of the FSS.

proposed FSS is placed between the ground plane and the radiator to expand the operating bandwidth by modifying the phase response of the reflection from the ground plane. Acting both as a balun and as an impedance transformer, the microstrip-based tapered balun is vertically inserted into the radiator and connected with the radiator arm through solder joints. It enables the radiator to be fed by a 50 Ω unbalanced cable without complex external baluns or cable organizers. A PTFE-based superstrate is placed above the bow-tie antenna to enhance the polarization purity. The geometric parameters of these critical components are listed in Table 1 (more details of design principles and processes are presented in the following sections).

B. RADIATOR

The geometries of the radiator employed in this design are presented in Fig. 2(a). To decrease the lower bound of the operating frequency band, the capacitive strength between the neighboring elements is enhanced by adopting a 25mil Rogers RO3010 ($\varepsilon_r = 11.2$, $tan\ \delta = 0.0022$ @ $10\ GHz$) board as the substrate. A floating copper plate is applied on the backside of the radiator to increase the coupling strength, induced by parallel plate capacitors generated by the overlapping between the radiator and the plate.

The radiator is excited by a 150 Ω discrete port and simulated in CST with unit-cell boundary conditions. The simulation results are shown in Fig. 2(b). It can be observed that the ideally fed radiator without a ground plane can achieve a broad bandwidth of 38.1:1 with radiation efficiency greater than 91% across the whole band.

C. FSS

In practice, the operating bandwidth will be significantly reduced by the reflection from the ground plane. As a result, the upper bound of the operational band is limited to $fmax = c/2h$ due to the reflection [12], which is given by:

$$Z_{ground} = j\eta_0 tan(\beta h) \tag{1}$$

where η_0, β, and h are the free space impedance, free space propagation constant, and distance between the ground plane and the radiator, respectively. It can be observed that when $f = c/2h$, the impedance Z_{ground} becomes zero, which means the radiator is short-circuited by the ground plane. Thus, the operating bandwidth is limited by the reflection.

To eliminate the short circuit and increase the operating bandwidth, in this paper, a method is presented to address these issues by introducing the low-loss phase-modulated FSS. The topology of the proposed FSS is depicted in Fig. 3.

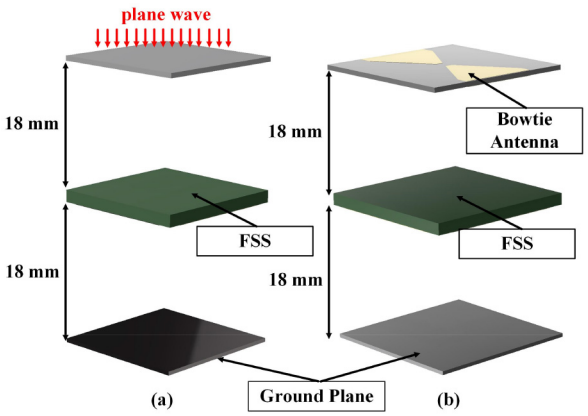

FIGURE 4. (a) The simulation model of the FSS excited by the plane wave. (b) The simulation model of the FSS excited by the proposed bow-tie antenna.

It is designed on a 62mil Rogers RT/duriod 5870 ($\varepsilon_r = 2.33$, $tan\ \delta = 0.0012\ @\ 10\ GHz$) board.

In general, the proposed FSS can eliminate the short circuit effects by modifying the phase rather than changing the magnitude of the reflected signal through resistive absorption. The shunt impedance can be calculated as:

$$Z_{ground} = j\eta\ tan(\Phi) \tag{2}$$

where Φ is the phase response of the reflected signal. In this case, phase difference Φ and distance h are no more linear dependent due to the FSS. The relationship between the phase difference Φ and the structures of FSS can be examined through the simulation setup shown in Fig. 4(a). As exhibited, the normally incident plane wave (TE_{00} or TM_{00} mode) is coming in with the distance $h = 18\ mm$ beyond the FSS. And the ground plane is also positioned 18 mm beneath the FSS to reflect the incoming wave. It is found that the parameter *fssw1* (as labeled in Fig. 3) is related to the phase difference Φ. The simulated phase responses of return loss (i.e., reflected signal) based on unit-cell boundary conditions with different values of *fssw1* are plotted at the top of Fig. 5. It is clear that the FSS can eliminate the short-circuit effect by avoiding the phase $\Phi = \pm k\pi$ (e.g., the phase will be around $\pm k\pi$ at 4 GHz without FSS). As shown in Fig. 4(b), to reveal the relationship between the phase response and the operating bandwidth, the bow-tie radiator discussed in the previous section is applied and simulated with a 150 Ω discrete port and unit-cell boundary conditions. The comparisons between the broadside active VSWRs of the immaculately fed antenna element with different values of *fssw1* are shown at the bottom of Fig. 5. As presented, without the low-loss FSS, the short circuit can be clearly observed at around 4 GHz, limiting the operating bandwidth. Whereas, the low-loss FSS can almost double the bandwidth by preventing the short circuit at $f = c/2h$. According to Fig. 5, it can be observed that when *fssw1* goes smaller from 0.9 mm to 0.4 mm, the absolute maximum value of the phase difference Φ becomes smaller, leading to a better wideband impedance matching. Eventually, when

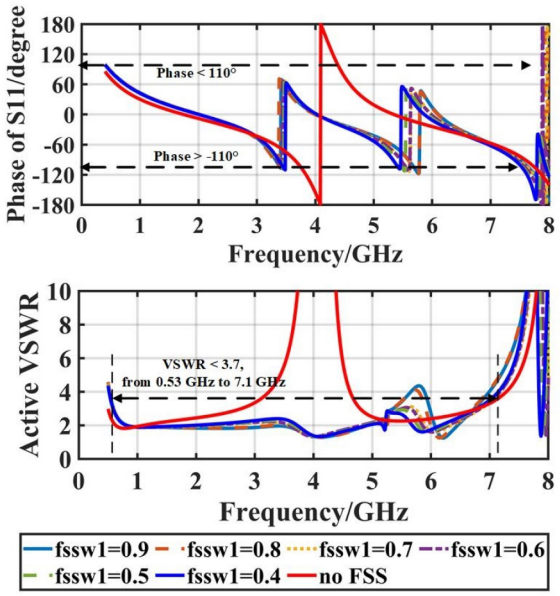

FIGURE 5. Top: phase response of the return loss when FSS is excited by the plane wave. Bottom: the broadside active VSWRs when FSS is excited by the proposed bow-tie antenna.

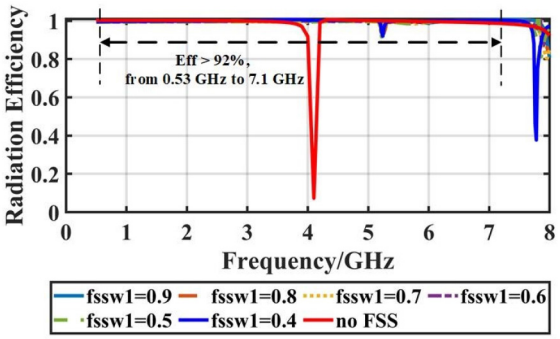

FIGURE 6. The radiation efficiency of the infinite array presented in Fig. 4(b).

fssw1 reaches 0.4 mm, the absolute phase response becomes smaller than 110°, and an operating bandwidth of 13.4:1 (from 0.53 GHz to 7.1 GHz) with VSWR < 3.7 is obtained.

To quantify how the FSS will affect the radiation efficiency, the following analytical equation can be applied [12]:

$$e_r = \frac{P_{raidated}}{P_{total}} = \frac{P_R}{P_G + P_R} = \frac{1}{\frac{P_G}{P_R}+1} = \frac{1}{\frac{\varepsilon_G}{\varepsilon_R}+1} \tag{3}$$

where ε_G and PG depend only on FSS parameters, and ε_R is associated with the superstrate. In this design, PG is small because the proposed FSS is low-loss, indicating the theoretical radiation efficiency e_r will not be reduced across the whole band. As exhibited in Fig. 6, the radiation efficiency of the proposed array (assuming an infinite array) is all above 92% across the entire band with different values of *fssw1*.

D. FEEDING STRUCTURE

As presented above, the designed antenna element excited by a perfect discrete port can achieve a large bandwidth

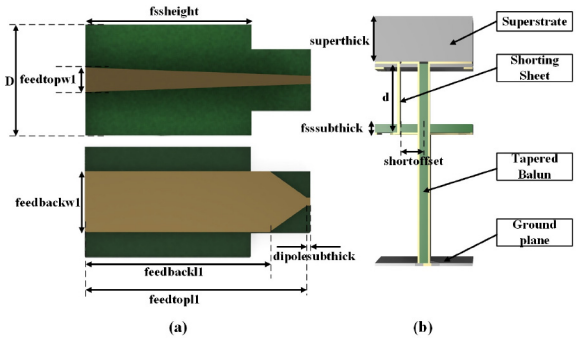

FIGURE 7. (a) The geometries and parameters of the balun. (b) Cross-section view of the proposed antenna element.

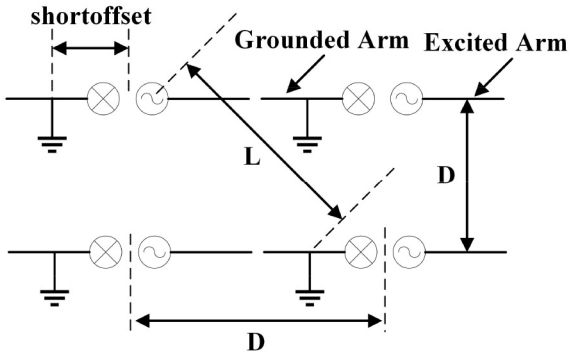

FIGURE 8. Top view of the antenna array model.

with high radiation efficiency. To feed this antenna array with a practical feeding structure, a microstrip-based tapered balun along with the shorting sheet is introduced in this design. The tapered balun, known as microstrip-to-parallel strip transition, is one of the most widely used baluns for ultra-wideband antennas such as spiral antennas [20]–[22] and ultra-wideband antenna arrays in [23] and [24]. It can provide suitable impedance transformation over a broad bandwidth and convert a single-ended port to a symmetric port to enable the antenna fed by 50 Ω unbalanced coaxial cables.

As presented in Fig. 7, the tapered balun, whose total length is 36.635 mm, is realized on a 62mil Rogers RT/duriod 5870 ($\varepsilon_r = 2.33$, $tan\ \delta = 0.0012$ @ $10\ GHz$) board. The first part of the tapered balun is a parallel stripline whose characteristic impedance is 150 Ω. This parallel stripline will be vertically connected with the radiator's arms. The other part is a microstrip line with a characteristic impedance of 50 Ω. Smooth impedance transformation from 50 Ω to 150 Ω is realized by linearly tapering the ground plane and the feed line of the microstrip line into the parallel strips. Compared with the Klopfenstein and exponentially tapered baluns, the linear tapered balun is much easier to design. It is noted that the 180-degree phase difference through the two sides of the feeding structure and the radiator will induce the common-mode, which resonates within the operating band and restricts the operating bandwidth [25]. To expand the operating bandwidth, one copper shorting sheet is applied and optimized to shift the common-mode out of the desired band by connecting one arm of the radiator with the ground plane. As shown in Fig. 7(b), the shorting sheet is connected from the radiator arm to the backed ground plane of the tapered balun with solder joints.

A top view of the array circuit model is illustrated in Fig. 8, which shows the placement of the shorting sheets along with the antenna arms [9]. In the proposed design, the common-mode of the antenna array with shorting sheets can be pushed above the operating band by:

$$f_{cm} \approx \frac{c_0}{2\sqrt{\varepsilon_r}\sqrt{D^2 + (D - shortoffset)^2}} \tag{4}$$

where f_{cm} is the resonant frequency of the common-mode, c_0 is the speed of light in vacuum, ε_r is the relative dielectric constant of the substrate, D is the length of the square unit cell, and *shortoffset* is the distance between the shorting sheet and the feeding center. To shift the f_{cm} out of the desired band, the value of the distance *shortoffset* can be estimated from (4) and verified with simulations. In the presented design, when the *shortoffset* is defined as 5.2 mm, the common-mode frequency is shifted to 7.2 GHz, positioned outside the operating band of the ideally fed infinite array shown in the previous section.

The length of the shorting sheet can also affect the operating bandwidth. The impedance of the shorting sheet is given by: $Z_{short} = Z_0 \tan(\frac{2\pi}{\lambda} d)$, where d is the length of the shorting sheet. It can be found Z_{short} will be infinite if d is a quarter-wavelength of a specific frequency f. Thus, the shorting sheet will not work at frequency f and the upper bound of the operating bandwidth will be cut down to $f = c/4d$. To shorten the length d and shift the open circuit out of the operating band, one square metal plate is designed on the FSS plane and vertically connected with the ground plane of the tapered balun as shown in Fig. 7(b). The ground plane is connected with the radiator by the shorting sheet and the metal plate. Thus, the length of the shorting sheet d can be easily modified by shifting the FSS up and down. The simulated broadside active VSWRs and the radiation efficiency of the infinite array with different lengths of the shorting sheet d are shown in Fig. 9. It can be observed that the operating bandwidth of 13.5:1 (from 0.53 GHz to 7.15 GHz) with VSWR < 3.3 and radiation efficiency higher than 94% can be achieved when the length d is 12 mm.

E. SUPERSTRATE

It is worth mentioning that the introduction of the FSS may affect the polarization purity. It is shown here that a complimentary superstrate can alleviate this issue. As presented in [12], it is known that the superstrate can draw the input power to the radiation loads and away from the resistive loads to improve the radiation efficiency, which means it can also be capitalized on to increase the polarization purity in a similar way. The equivalent circuit model of the proposed antenna array is presented in Fig. 10(a). To quantify how

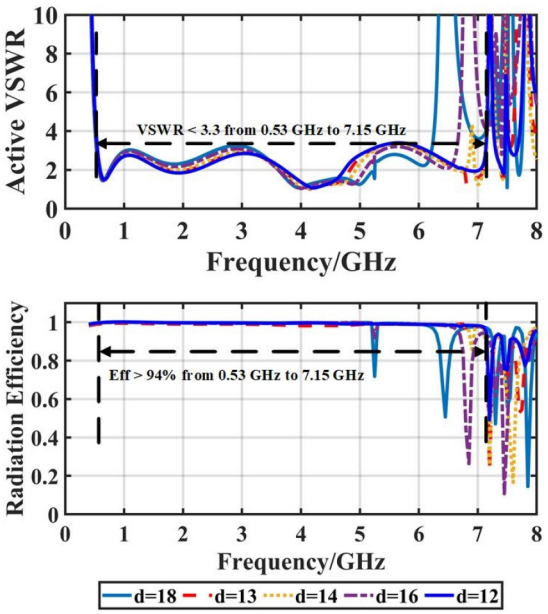

FIGURE 9. The simulated broadside active VSWRs (top) and radiation efficiency (bottom) with different lengths of the shorting sheet (i.e., d (unit: mm)).

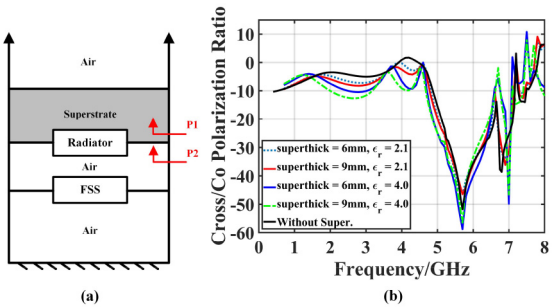

FIGURE 10. (a) The equivalent circuit of the antenna array. (b) Simulated polarization purity of the proposed infinite array with different superstrates.

the FSS and the superstrate will affect the polarization purity *PR*, the following analytical equation can be applied:

$$PR = \frac{P_{co}}{P_{cross}} = \frac{P1_{co} + P2_{co}}{P2_{cross}} = \frac{1 - P2_{cross}}{P2_{cross}} \tag{5}$$

where *P1* is the power transmits to the radiation load directly, *P2* is the power reflected by the ground plane. Usually, it is known that $P1 + P2 = 1$. Since the input power can be drawn to the radiation loads by the superstrate, *P1* can be increased so that $P2_{co}$ and $P2_{cross}$ will be decreased proportionally. In this way, the properly designed superstrate can enhance polarization purity.

In Fig. 10(b), the relationships between the polarization purity and the superstrates with different thicknesses and relative dielectric constant are given. As presented, the design parameter ε_r and the *superthick* labeled in Fig. 7 are relative dielectric constant and thickness of the superstrate. It can be observed that the polarization purity is not favorable at 4.1 GHz without the superstrate, which is higher than 0 dB. The introduced superstrates can significantly improve the polarization purity. Especially, when an $\varepsilon_r = 2.1$, $superthick = 9\ mm$ superstrate is used, the cross/co polarization ratio at 4.1 GHz band is significantly reduced, and the polarization purity maintains good at the higher frequency band (e.g., 6.7 GHz). The polarization purity will deteriorate at around 6.7 GHz when other superstrates with higher dielectric constants are used. In general, with this superstrate (i.e., $\varepsilon_r = 2.1$, $superthick = 9\ mm$), the cross/co polarization can be less than −1.5dB across the whole band and less than −5dB across most of the operating frequency band.

For many high-resolution radar systems or imaging systems, the most important specs are the radiated power and the operating bandwidth. The larger bandwidth and the higher radiated power can provide these systems with higher resolution and a more extensive detection range. In those cases, polarization purity is not as crucial as radiation efficiency and operating bandwidth (e.g., for radar systems, the received power will be critical for radar performance) because good polarization purity is not required to avoid orthogonal polarization coupling or crosstalk.

It has been proved that it is impossible to realize a tightly coupled antenna array with extremely broad bandwidth, low-profile, high radiation efficiency, and high polarization purity [26], [27] because either the magnitude or the phase of the reflection from the ground needs to be modified. In [26], the bandwidth limits of lossless reciprocal PEC backed planar antenna array under arbitrary polarization are discussed. From [26], an absolute upper limit regardless of polarization is given by:

$$I_{max} = \pi L_{TM} + \pi L_{TE} \tag{6}$$

where I_{max} is an upper bound for the integral,

$$\int_0^{w_0} w^{-2} log\left|\frac{1}{S_{11}(jw)}\right| dw \ll I_{max} \tag{7}$$

L_{Ti} is interpreted as the effective ground plane inductance, and w_0 presents the operating bandwidth. It is shown in (6) that the maximum possible impedance bandwidth of a lossless reciprocal antenna array with arbitrary polarization is twice that of the same array with constant polarization, which is consistent with our proposed antenna array.

III. FINITE ARRAY PERFORMANCE

To illustrate the performance of the designed TCDA, an infinite array based on it is simulated with unit-cell boundary conditions. The simulated active VSWRs under broadside and scanned conditions are presented at the top of Fig. 11. As indicated, this design can achieve a bandwidth of 13.66:1 (0.52 GHz – 7.10 GHz) with active VSWR < 2.49 at broadside. When the infinite array is scanned down to 45° in the E-plane (as labeled in Fig. 1), it can operate from 0.53 GHz to 7.02 GHz (13.2:1) with active VSWR < 2.62. When scanned down to 45° in the H-plane, it can achieve a bandwidth of 0.50 GHz – 6.13 GHz (12.2:1) with active VSWR < 4.5. And the active VSWR will decrease to 3.3 when scanned to 45° in the D-plane across 0.53 GHz – 5.42 GHz

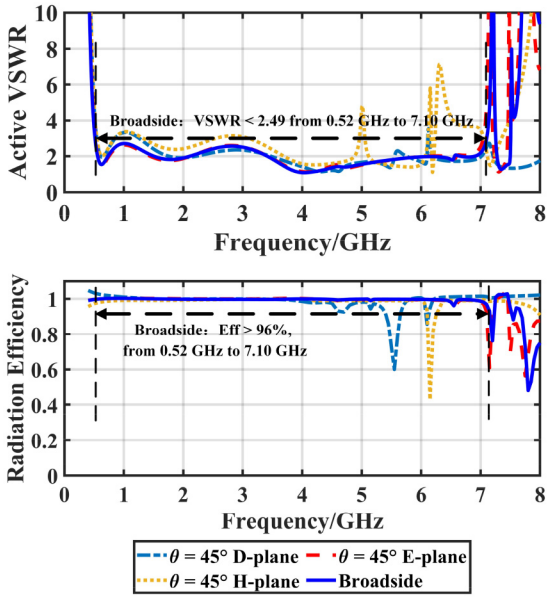

FIGURE 11. Simulated active VSWRs (top) and radiation efficiency (bottom) of the infinite antenna array under broadside and scanned conditions.

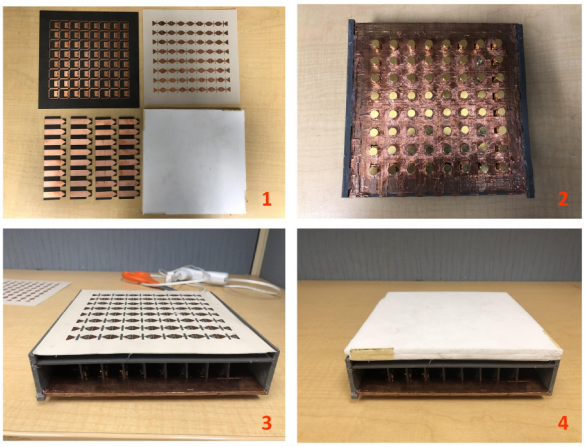

FIGURE 12. Photos of the fabricated 8×8 array prototype.

(10.3:1). Fig. 11 also presents the radiation efficiency of the infinite array when it is at broadside or scanned to 45 ° in the E-, H- and D-plane. It can be observed that the radiation efficiency is above 85% across the proposed band in all these cases.

IV. RESULTS OF AN 8 × 8 PROTOTYPE ARRAY

A. OVERVIEW OF THE PROPOSED ANTENNA ARRAY ELEMENTS

To further validate the proposed design concepts, an 8 × 8 array prototype was fabricated and characterized experimentally. Photos of the prototype at four various stages of the assembling process are shown in Fig. 12. As shown in Fig. 12(1), 64 radiator elements and 64 FSS elements are fabricated on a 180 mm × 180 mm Rogers RO3010 board and a 180 mm × 180 mm Rogers RT/duriod 5870 board, separately. Eight tapered baluns are fabricated together as

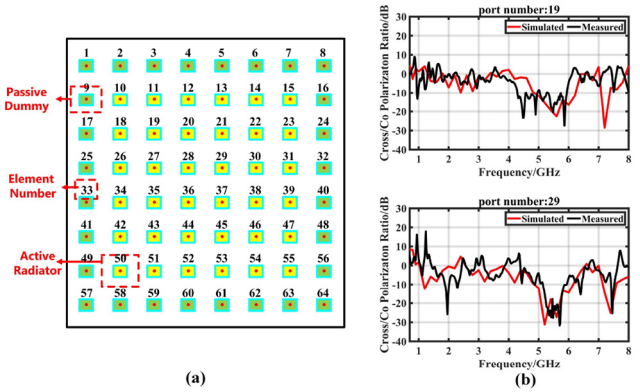

FIGURE 13. (a) Elements distribution of the antenna array. (b) Simulated and measured cross-co polarization ratios of two randomly picked antenna elements.

one row on a 144 mm × 36.625 mm Rogers RT/duriod 5870 board, and a feeding array formed by 8 identical rows is employed to feed the array. Moreover, 64 copper sheets of 5 mm width, 9.7 mm length and 1.5 mm thickness are used to connect the ground plane with the radiators as the shorting sheets. As depicted in Fig. 12(2), one polylactic acid (PLA, $\varepsilon_r = 3.11$, $tan\ \delta = 0.013$) plate of 180 mm × 180 mm is designed and fabricated by a 3D printer. Copper tapes of 0.2 mm thickness are used and coated on the PLA plate to form the ground plane and reflect the incident wave. It is worth mentioning that, compared with the traditional way to develop the ground plane using large metal boards, 3D printing is a much more convenient and economical solution. It can be easily customized and has a higher resolution, making the gaps between the ground plane and the SMA connectors smaller so that very little power will be transmitted. As shown in Fig. 12(3), to facilitate the assembling of the prototype, two PLA side walls with three grooves are designed and printed by the printer as a robust framework. The radiators board, the FSSs board, and the ground board can tightly insert into these grooves. Also, the distances among these three planes are fixed and consolidated by the printed frame. In Fig. 12(4), the 9 mm PTFE board is positioned above the radiators as the superstrate. Hot melt adhesive is used to immobilize the superstrate and increase the stability of the prototype.

B. SIMULATIONS AND MEASUREMENT RESULTS OF THE 8×8 ARRAY PROTOTYPE

For tightly coupled arrays, only elements surrounded by others can work appropriately due to the edge truncation [28]. To decrease the edge truncation effect in the simulation, only the central 6 × 6 elements are excited simultaneously with 50 Ω waveguide ports. The peripheral 28 elements assigned with waveguide ports but without excitation are configured as perfect matched load. The elements distribution of the fabricated antenna array is shown in Fig. 13(a). To characterize the radiation pattern of the fabricated prototype, a similar protocol is applied to conduct the measurements. The peripheral 28 elements in the prototype are terminated

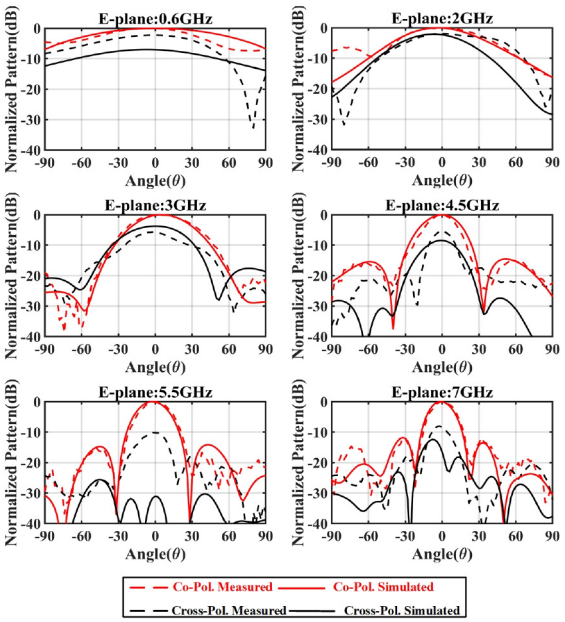

FIGURE 14. The radiation pattern of the prototype in the E-plane.

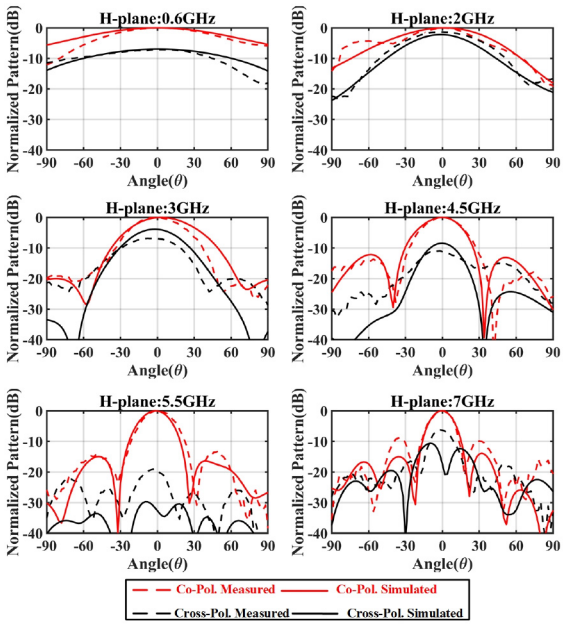

FIGURE 15. The radiation pattern of the prototype in the H-plane.

with 50 Ω matching loads as dummy elements [31]. The unit excitation active element pattern method [32] is applied for all central 36 active elements to characterize the radiation pattern in the E-, H- and D- planes. The comparisons between the simulated and measured cross-co polarization ratios of two randomly selected embedded elements (which are element 19 and element 29 shown in Fig. 13(a)) are presented in Fig. 13(b). Good agreement has been achieved between the simulations and the measurements.

The comparisons between the normalized simulated radiation pattern and the normalized characterized pattern in the E-, H- and D-plane are shown in Fig. 14, Fig. 15, and

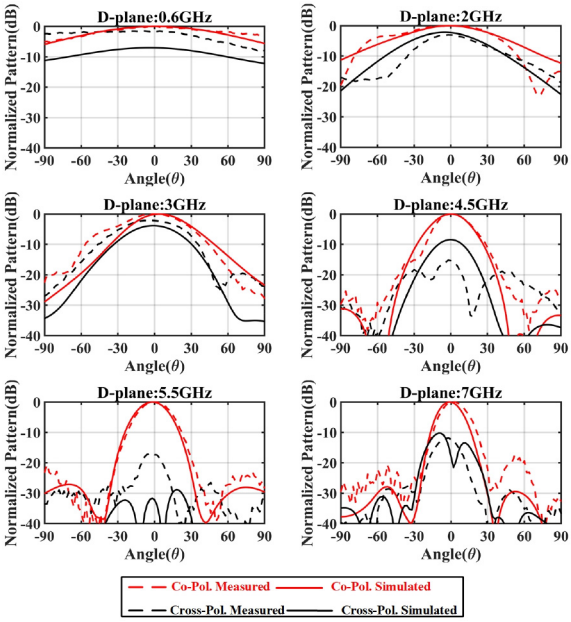

FIGURE 16. The radiation pattern of the prototype in the D-plane.

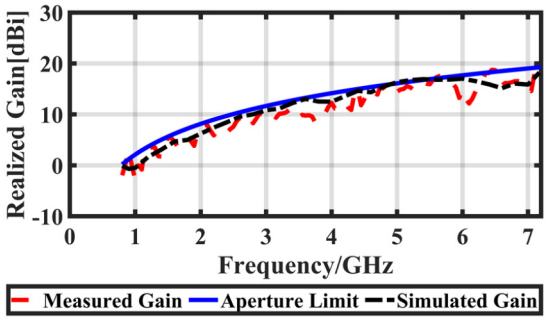

FIGURE 17. Realized gain of the prototype vs. frequency.

Fig. 16, respectively. Good agreements between the numerical simulations and the measurements can be observed. Fig. 17 presents the measured realized gain, simulated realized gain, and the aperture limits (Aperture Limits $= 4\pi \frac{A}{\lambda^2}$, A is the aperture size of the 6 × 6 active antenna array). It can be observed that they are also in good agreement. Please note that gain measurements are only presented for frequencies greater than 700 MHz due to the low-frequency cutoff of our chamber.

Table 2 compares the performances of the proposed antenna array with state-of-the-art arrays reported in the literature. The TCAs presented in [8]–[10], [16], [18], [19] and [29] show good performances, but the operating bandwidth is still limited by the reflection (bandwidth is less than 10:1). Our proposed array has a larger bandwidth (13.66:1). Compared with the works shown in [12], [14], and [30] which utilize lossy resistive sheets to absorb the reflection, the reported low-loss FSS-based array can achieve a comparable operating bandwidth with much higher radiation efficiency (increased by 23% or more).

TABLE 2. Comparative study of proposed antenna array with other TCAs.

Antenna Literature	Profile	Bandwidth	Radiation Efficiency	Scanning Angle	Feeding structure
[8]	$0.43\lambda_{high}$	3:1	>90%	±45°	Unbalanced lines with shorting vias
[9]	$0.33\lambda_{high}$	5:1	>90%	±45°	Unbalanced lines with shorting vias
[10]	$0.48\lambda_{high}$	6:1	95% on average	±60°	Unbalanced lines with shorting vias
[12]	$1.15\lambda_{high}$	21:1	>73%	----	Twin coaxial lines
[14]	$1.56\lambda_{high}$	13.9:1	>60%	±45°	Stripline-based folded Marchand balun
[15]	$1.39\lambda_{high}$	20.9:1	>92%	±30°	Balun chip (MABA-010247-2R1250)
[16]	$0.92\lambda_{high}$	9:1	85% on average	±60°	Stripline-based Marchand balun
[17]	$1.93\lambda_{high}$	28:1	83% on average	±60°	Klopfenstein tapered balun
[18]	$0.48\lambda_{high}$	5.5:1	>78% when scanned	±70°	Klopfenstein tapered balun with shourting structure
[19]	$0.62\lambda_{high}$	5.13:1	>64% when scanned	±70°	Microstrip-to-slotline structure with shorting structure
[29]	$0.78\lambda_{high}$	6.5:1	----	±70°	Stripline-based Marchand balun
[30]	$3.41\lambda_{high}$	46:1	72% on average	±45°	Stripline-based tapered balun
This work	$1.08\lambda_{high}$	13. 66:1	>96%	±45°	Linear tapered balun with shorting structure

Table 2 also summarizes the feeding structures of the arrays. The works presented in [8]–[10] can be fed by unbalanced feeding structures without any internal or external baluns. Nevertheless, these feeding structures limit the operating bandwidth of these arrays. The feeding structures in [14], [16], and [29] are all stripline-based folded Marchand baluns. Compared with these works, the presented design can provide a more convenient and cost-saving feeding structure with broader bandwidth. The feeding schemes presented in [18] and [19] are based on microstrip transmission lines with shorting structures. Nonetheless, these shorting structures are connected from the ground plane to the radiator's arm directly, which will be an open circuit and limit the operating bandwidth if the distance between the ground plane and the radiator plane is enlarged. Comparing with these feeding structures, our proposed feeding structure has great application potentials in the ultra-wideband antenna array. Compared with the TCDA based on polarization converter and balun chip shown in [15], our proposed antenna array can alleviate the issue of poor polarization purity bandwidth in the whole operating band. Additionally, the integrated balun adapted in our design can have higher efficiency, better scalability, and better power handling proprieties compared with the discrete balun chip.

V. CONCLUSION

A new low-profile tightly coupled antenna array with a low-loss FSS and an integrated feeding is presented. The proposed array achieved an operating bandwidth of 13.66:1(0.52 GHz – 7.10 GHz, VSWR $<$ 2.49) and simulated radiation efficiency higher than 96%. By introducing the FSS, the array's bandwidth has been significantly increased without decreasing its radiation efficiency. The microstrip-based feeding structure employed in this design enables the array element to be directly excited with a 50 Ω unbalanced coaxial cable. The proposed design concept has been verified through the measurements of an 8 × 8 array prototype. Good agreements have been achieved between simulation and measurement results. In general, the proposed wideband and high-efficiency antenna array can be adopted to high-power RF/microwave systems such as high-resolution, long-range radar systems and imaging systems, as well as many other wireless systems.

REFERENCES

[1] J.-B. Yan, S. Gogineni, B. Camps-Raga, and J. Brozena, "A dual-polarized 2–18-GHz vivaldi array for airborne radar measurements of snow," *IEEE Trans. Antennas Propag.*, vol. 64, no. 2, pp. 781–785, Feb. 2016.

[2] R. W. Kindt, J. T. Logan, and M. W. Elsallal, "Machined metal FUSE array apertures," in *IEEE Int. Symp. Phased Array Syst. Technol.*, Waltham, MA, USA, 2019, pp. 1–4.

[3] N. Wang, N. Ou, P. Wang, and R. Wang, "Ultra-wide band bowtie slot waveguide antenna array for SAR application," *IET Microw. Antennas Propag.*, vol. 13, no. 3, pp. 391–397, Feb. 2019.

[4] M. Li, R. Birken, N. X. Sun, and M. L. Wang, "Compact slot antenna with low dispersion for ground penetrating radar application," *IEEE Antennas Wireless Propag. Lett.*, vol. 15, pp. 638–641, 2016.

[5] M. Jones and J. Rawnick, "A new approach to broadband array design using tightly coupled elements," in *Proc. IEEE Mil. Commun. Conf.*, Orlando, FL, USA, 2011, pp. 1802–1807.

[6] B. Munk *et al.*, "A low-profile broadband phased array antenna," in *Proc. IEEE Antennas Propag. Soc. Int. Symp. Dig. Held Conjunction USNC/CNC/URSI North Amer. Radio Sci. Meeting*, Columbus, OH, USA, 2003, pp. 448–451.

[7] B. Munk, *Frequency Selective Surfaces, Theory and Design*. New York, NY, USA: Wiley, 2000, ch. 9, pp. 315–335.

[8] S. S. Holland, D. H. Schaubert, and M. N. Vouvakis, "A 7–21 GHz dual-polarized planar ultrawideband modular antenna (PUMA) array," *IEEE Trans. Antennas Propag.*, vol. 60, no. 10, pp. 4589–4600, Oct. 2012.

[9] S. S. Holland and M. N. Vouvakis, "The planar ultrawideband modular antenna (PUMA) array," *IEEE Trans. Antennas Propag.*, vol. 60, no. 1, pp. 130–140, Jan. 2012.

[10] J. T. Logan, R. W. Kindt, M. Y. Lee, and M. N. Vouvakis, "A new class of planar ultrawideband modular antenna arrays with improved bandwidth," *IEEE Trans. Antennas Propag.*, vol. 66, no. 2, pp. 692–701, Feb. 2018.

[11] W. Croswell, T. Durham, M. Jones, D. Schaubert, P. Friederich, and J. Maloney, "Wideband arrays," in *Modern Antenna Handbook*, C. A. Balanis, Ed. Hoboken, NJ, USA: Wiley, 2008, pp. 581–629.

[12] W. F. Moulder, K. Sertel, and J. L. Volakis, "Superstrate-enhanced ultrawideband tightly coupled array with resistive FSS," *IEEE Trans. Antennas Propag.*, vol. 60, no. 9, pp. 4166–4172, Sep. 2012.

[13] W. F. Moulder, "Novel implementations of ultrawideband tightly coupled antenna arrays," Ph.D. dissertation, Dept. Elect. Comput. Eng., Ohio State Univ., Columbus, OH, USA, 2012.

[14] W. F. Moulder, K. Sertel, and J. L. Volakis, "Ultrawideband superstrate-enhanced substrate-loaded array with integrated feed," *IEEE Trans. Antennas Propag.*, vol. 61, no. 11, pp. 5802–5807, Nov. 2013.

[15] S. Kim and S. Nam, "Characteristics of TCDA with polarization converting ground plane," *IEEE Trans. Antennas Propag.*, vol. 69, no. 4, pp. 2359–2364, Apr. 2021.

[16] J. Zhong, A. Johnson, E. A. Alwan, and J. L. Volakis, "Dual-linear polarized phased array with 9:1 bandwidth and 60° scanning off broadside," *IEEE Trans. Antennas Propag.*, vol. 67, no. 3, pp. 1996–2001, Mar. 2019.

[17] M. Carvalho, A. D. Johnson, E. A. Alwan, and J. L. Volakis, "Semi-resistive approach for tightly coupled dipole array bandwidth enhancement," *IEEE Open J. Antennas Propag.*, vol. 2, pp. 110–117, 2021.

[18] A. O. Bah, P.-Y. Qin, R. W. Ziolkowski, Y. J. Guo, and T. S. Bird, "A wideband low-profile tightly coupled antenna array with a very high figure of merit," *IEEE Trans. Antennas Propag.*, vol. 67, no. 4, pp. 2332–2343, Apr. 2019.

[19] C.-H. Hu, B.-Z. Wang, R. Wang, S.-Q. Xiao, and X. Ding, "Ultrawideband, wide-angle scanning array with compact, single-layer feeding network," *IEEE Trans. Antennas Propag.*, vol. 68, no. 4, pp. 2788–2796, Apr. 2020.

[20] T.-K. Chen and G. H. Huff, "Stripline-fed archimedean spiral antenna," *IEEE Antennas Wireless Propag. Lett.*, vol. 10, pp. 346–349, 2011.

[21] Y.-W. Zhong, G.-M. Yang, J.-Y. Mo, and L.-R. Zheng, "Compact circularly polarized archimedean spiral antenna for ultrawideband communication applications," *IEEE Antennas Wireless Propag. Lett.*, vol. 16, pp. 129–132, 2017.

[22] S.-G. Mao, J.-C. Yeh, and S.-L. Chen, "Ultrawideband circularly polarized spiral antenna using integrated balun with application to time-domain target detection," *IEEE Trans. Antennas Propag.*, vol. 57, no. 7, pp. 1914–1920, Jul. 2009.

[23] Z. Yao, W. Ren, Z. Xue, and W. Li, "The design of A 2-12GHz scaning tightly coupled dipole array," in *Proc. Int. Conf. Microw. Millimeter Wave Technol.*, Chengdu, China, 2018, pp. 1–3.

[24] T. Xia, S. Yang, and Z. Nie, "Design of a tapered balun for broadband arrays with closely spaced elements," *IEEE Antennas Wireless Propag. Lett.*, vol. 8, pp. 1291–1294, 2009.

[25] C. Lyu, S. Yang, H. Zhang, and Z. Nie, "A new type of tilted tightly coupled dipole arrays with two-dimensional scanning property," in *Proc. IEEE Int. Conf. Commun. Problem-Solving*, Guilin, China, 2015, pp. 51–53.

[26] J. P. Doane, K. Sertel, and J. L. Volakis, "Bandwidth limits for lossless, reciprocal PEC-backed arrays of arbitrary polarization," *IEEE Trans. Antennas Propag.*, vol. 62, no. 5, pp. 2531–2542, May 2014.

[27] J. P. Doane, K. Sertel, and J. L. Volakis, "Matching bandwidth limits for arrays backed by a conducting ground plane," *IEEE Trans. Antennas Propag.*, vol. 61, no. 5, pp. 2511–2518, May 2013.

[28] P. Khanal, J. Yang, M. Ivashina, A. Höök, and R. Luo, "Edge truncation effects in a wide-scan phased array of connected bowtie antenna elements," in *Proc. Eur. Conf. Antennas Propag.*, Copenhagen, Denmark, 2020, pp. 1–5.

[29] E. Yetisir, N. Ghalichechian, and J. L. Volakis, "Ultrawideband array with 70° scanning using FSS superstrate," *IEEE Trans. Antennas Propag.*, vol. 64, no. 10, pp. 4256–4265, Oct. 2016.

[30] A. D. Johnson, J. Zhong, S. B. Venkatakrishnan, E. A. Alwan, and J. L. Volakis, "Phased array with low-angle scanning and 46:1 bandwidth," *IEEE Trans. Antennas Propag.*, vol. 68, no. 12, pp. 7833–7841, Dec. 2020.

[31] E. Holzman, "On the use of dummy elements to match edge elements in transmit arrays," in *Proc. IEEE Int. Symp. Phased Array Syst. Technol.*, Waltham, MA, USA, 2013, pp. 549–552.

[32] D. F. Kelley and W. L. Stutzman, "Array antenna pattern modeling methods that include mutual coupling effects," *IEEE Trans. Antennas Propag.*, vol. 41, no. 12, pp. 1625–1632, Dec. 1993.

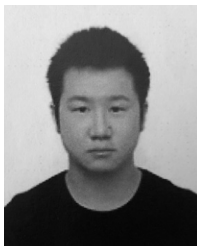

HONG TANG received the B.Sc. degree in optoelectronic information science and engineering from the Huazhong University of Science and Technology in 2017. He has been serving as a Research Assistant with UMASS Lowell since 2017. His current research interests include wideband antenna array, millimeter-wave systems, and flexible antennas.

BOWEN ZHENG received the B.Sc. degree in electronics engineering from Southeast University, Nanjing, Jiangsu, China, in 2014, and the M.Sc. degree in electronics engineering from the University of Maryland, College Park, MD, USA, in 2016. He is currently pursuing the Ph.D. degree in electronics engineering with the University of Massachusetts Lowell, Lowell, MA, USA. His research interests include the metasurfaces, radar and applications, antenna design, and RF metrology.

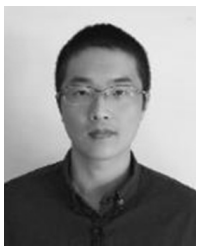

SENSONG AN received the bachelor's and master's degrees from Electrical Engineering and Information Science Department, University of Science and Technology of China in 2013 and 2016, respectively. He is currently pursuing the Ph.D. degree with EECE Department, University of Massachusetts Lowell. His research interests are in the area of microwave and THz technology, meta-optic design and inverse design approaches enabled by machine learning techniques.

HANG LI received the B.Sc. degree in physics from Jilin University in 2012. She is currently pursuing the Ph.D. degree in electrical engineering with the University of Massachusetts Lowell. Her current research interests include electromagnetic metamaterials, terahertz metasurface, and optoelectronic device fabrication.

MOHAMMAD HAERINIA received the B.Sc. and M.Sc. degrees in electrical engineering from Shahid Beheshti University, Tehran, Iran, in 2014 and 2016, respectively, and the second M.Sc. degree in biomedical engineering from the University of North Dakota, ND, USA, in 2019. He is currently pursuing the Ph.D. degree in electrical engineering with the University of Massachusetts Lowell, MA, USA. His research interest includes multidisciplinary areas of applied electromagnetics, including medical optics, metasurfaces, wireless power transfer (WPT), and WPT for medical applications.

CLAYTON FOWLER received the B.S. degree in physics and mathematics from the University of Utah, the M.S. degree in medical physics from Columbia University, and the Ph.D. degree in applied physics from the University of South Florida. He is a Postdoctoral Research Associate with the Electrical and Computer Engineering Department, University of Massachusetts Lowell. His research interests include metamaterials, photonics, optics, optoelectronics, and machine learning. He is a member of APS and OSA.

HUALIANG ZHANG (Senior Member, IEEE) received the B.S. degree in electrical engineering from the University of Science and Technology of China in 2003, and the Ph.D. degree in electrical and computer engineering from the Hong Kong University of Science and Technology in 2007. From 2007 to 2009, he was a Postdoctoral Research Associate with the University of Arizona. From 2009 to 2016, he was an Assistant Professor and then an Associate Professor with the University of North Texas. He is currently a Professor with the Electrical and Computer Engineering Department, University of Massachusetts Lowell. He has coauthored over 200 journal and conference papers. His research interests include antennas, RF/microwave/millimeter-wave circuits and systems, metasurfaces and metamaterials, nano-photonics, and optoelectronics in both rigid and flexible substrates, as well as their applications, covering the frequency range from RF/microwave and THz to infrared and visible. He serves as the Sub-Committee Chair of the IEEE International Microwave Symposium and Technical Committee Members of several major technical conferences, as well as an Associate Editor of *International Journal of Numerical Modelling: Electronic Networks, Devices and Fields*.